PAPER • OPEN ACCESS

Density perturbation mode structure of high frequency compressional and global Alfvén eigenmodes in the National Spherical Torus Experiment using a novel reflectometer analysis technique

View the article online for updates and enhancements.

Related content

- High spatial sampling global mode structure measurements via multichannel reflectometry in NSTX
  N A Crocker, W A Peebles, S Kubota et al.

- Internal amplitude, structure and identification of compressional and global Alfvén eigenmodes in NSTX
  N.A. Crocker, E.D. Fredrickson, N.N. Gorelenkov et al.

- Energetic particle physics in fusion research in preparation for burning plasma experiments
  N.N. Gorelenkov, S.D. Pinches and K. Toi

Density perturbation mode structure of high frequency compressional and global Alfvén eigenmodes in the National Spherical Torus Experiment using a novel reflectometer analysis technique

N.A. Crocker[1] , **S. Kubota**[1]**, W.A. Peebles**[1]**, T.L. Rhodes**[1]**, E.D. Fredrickson**[2]**, E. Belova**[2]**, A. Diallo**[2]**, B.P. LeBlanc**[2] **and S.A. Sabbagh**[3]

[1] Univ. of California, Los Angeles, CA 90095, United States of America
[2] Princeton Plasma Physics Laboratory, Princeton, NJ 08543, United States of America
[3] Dept. of Applied Physics and Applied Mathematics, Columbia Univ., New York, NY 10027, United States of America

E-mail: ncrocker@physics.ucla.edu

CrossMark

Abstract

Reflectometry measurements of compressional (CAE) and global (GAE) Alfvén eigenmodes are analyzed to obtain the amplitude and spatial structure of the density perturbations associated with the modes. A novel analysis technique developed for this purpose is presented. The analysis also naturally yields the amplitude and spatial structure of the density contour radial displacement, which is found to be 2–4 times larger than the value estimated directly from the reflectometer measurements using the much simpler 'mirror approximation'. The modes were driven by beam ions in a high power (6 MW) neutral beam heated H-mode discharge (#141398) in the National Spherical Torus Experiment. The results of the analysis are used to assess the contribution of the modes to core energy transport and ion heating. The total displacement amplitude of the modes, which is shown to be larger than previously estimated (Crocker *et al* 2013 *Nucl. Fusion* **53** 43017), is compared to the predicted threshold (Gorelenkov *et al* 2010 *Nucl. Fusion* **50** 84012) for the anomalously high heat diffusion inferred from transport modeling in similar NSTX discharges. The results of the analysis also have strong implications for the energy transport via coupling of CAEs to kinetic Alfvén waves seen in simulations with the Hybrid MHD code (Belova *et al* 2015 *Phys. Rev. Lett.* **115** 15001). Finally, the amplitudes of the observed CAEs fall well below the threshold for causing significant ion heating by stochastic velocity space diffusion (Gates *et al* 2001 *Phys. Rev. Lett.* **87** 205003).

Keywords: Alfvén eigenmodes, energetic ions, plasma heating, plasma transport, wave-particle interactions, reflectometry

(Some figures may appear in colour only in the online journal)

1. Introduction

Fast-ions (e.g. fusion alphas and neutral beam ions) will potentially excite high frequency compressional (CAE) and global (GAE) Alfvén eigenmodes in ITER or a Fusion Nuclear Science Facility device [1]. High frequency AEs have been shown to cause fast-ion transport [2–4], to correlate with anomalous electron thermal transport [5], to contribute to ion heating [6], and are postulated to cause energy transport [7–10] via several different mechanisms.

A novel analysis technique is developed and applied to previously reported [11, 12] reflectometry measurements in order to obtain the density perturbation (δn) amplitude and structure of CAEs and GAEs in a high power (6 MW), beam-heated H-mode plasma (discharge # 141398) in the National Spherical Torus Experiment (NSTX) [13] with anomalous core energy transport similar to those discussed in [5]. Reflectometry has a long history of use as a diagnostic for measuring the internal amplitude and spatial structure of large scale density perturbations. A common approximation has been to assume that the reflectometer fluctuation measurements are localized to the cutoff, or the point of reflection of the microwaves (e.g. [14, 15]). Specifically, it is assumed that the measurements result purely from the motion of the cutoff caused by density perturbations in the vicinity of the cutoff. However, analysis techniques have been developed that seek greater accuracy by combining measurements from reflectometers with different frequencies, taking into account the nonlocal response of the reflectometers, (see e.g. [16–18] for different approaches). Such techniques involve inverting the set of reflectometer measurements to obtain a density perturbation with a spatial structure and amplitude that simultaneously explains all the measurements of the set. Such techniques take into account the contribution of propagation through the density perturbation along the full path between antenna and cutoff. The inversion technique presented here seeks to improve upon previously developed techniques of this variety. The values of δn obtained via this inversion can differ significantly from local approximation estimates. These values of δn are valuable because they can be used to derive estimates of the mode magnetic perturbation (δb), which can then be used in conjunction with theory to predict the contribution of the modes to ion heating, as well as energy transport via several different hypothesized mechanisms. In particular, these estimates can be used to predict electron thermal transport via electron orbit stochastization [7] and ion heating rate via stochastic velocity space diffusion [6]. The inversion results can be also used to facilitate prediction of energy transport via coupling of CAEs to kinetic Alfvén waves [9, 10].

Section 2 describes the plasma in which the reflectometer measurements were made. Section 3 describes the analysis technique developed to obtain δn from the reflectometer measurements and presents the results of the analysis. Section 4 presents discussion and conclusions.

2. Plasma conditions

The reflectometry measurements analyzed here [11, 12] were obtained in an NSTX deuterium discharge (#141398) with a current (I_P) of 800 kAmp (figure 1(*a*)) and a magnetic field of 0.32 T at the magnetic axis ($R_0 \approx 1.05$ m) that was heated with 6 MWs of injected deuterium neutral beam power. The temporal evolution of the discharge is shown in figure 1, with the time at which the measurements were obtained ($t = 580$ ms) marked by a dashed vertical line. Figure 1(*b*) shows the injected power (P_{NB}) versus time for each of the three sources on NSTX (A: $R_{TAN} = 69.4$ cm; B: $R_{TAN} = 59.2$ cm; C: $R_{TAN} = 48.7$ cm). Figure 1(*c*) shows the measured rate (r_{NEUT}) of D–D fusion neutron production from a combination of beam–beam and beam-target interactions. Figure 1(*d*) shows the plasma safety factor at the magnetic axis (q_0) and the flux surface containing 95% of the total poloidal flux (q_{95}), obtained by reconstruction of the equilibrium magnetic field via the EFIT code using external magnetic measurements for constraints, as well as partial kinetic pressure profile information and a diamagnetic loop measurement [19–21]. Figure 1(*e*) shows the lower divertor deuterium Balmer-α (Dα) emission, which abruptly drops substantially around $t = 180$ ms due to a transition from L-mode (low confinement) to H-mode (high confinement). Figures 1(*f*) and (*g*) show the plasma density (n_e) and temperature (T_e) respectively, from Multipoint Thomson Scattering [22]. In each panel, the peak and line average values are shown, where the latter is an average over major radius in the plasma midplane.

The density profile of the plasma at the time of the reflectometer measurements is shown in figure 2. As noted in [11, 12], the reflectometer measurements were obtained with a 16 channel fixed-frequency array with frequencies spread over 30–75 GHz, operating with ordinary-mode polarization, leading to cutoff densities of 1.1–6.9×10^{13} cm^{-3} [11] (figure 2). The cutoff positions for O-mode polarized microwaves are shown for each of the frequencies in the array used for the measurements [11]. The locations of magnetic axis ($R_0 \approx 1.05$ m) and last closed flux surface ($R_{LCFS} \approx 1.46$ m) from EFIT reconstruction of the equilibrium are shown. As discussed in [11], the profile shown is a fit to the measured n_e with a smoothing, or curvature minimizing spline, and the n_e data is rescaled to best fit observed reflection onset times for select channels of the reflectometer array. The rescaling is necessitated by a coating on the viewing window used by the Multipoint Thomson scattering diagnostic (MPTS). This particular time is the focus of the analysis because of the availability of the MPTS measurements and the unique range of reflectometer coverage enabled by the density profile. As can be seen in figure 1, central density rises through most of the discharge, only beginning to fall after $t \sim 1100$ ms. The time of analysis is the first time in the discharge where MPTS data, which is acquired every 16.7 ms, is available and all reflectometer channels are reflecting from the plasma.
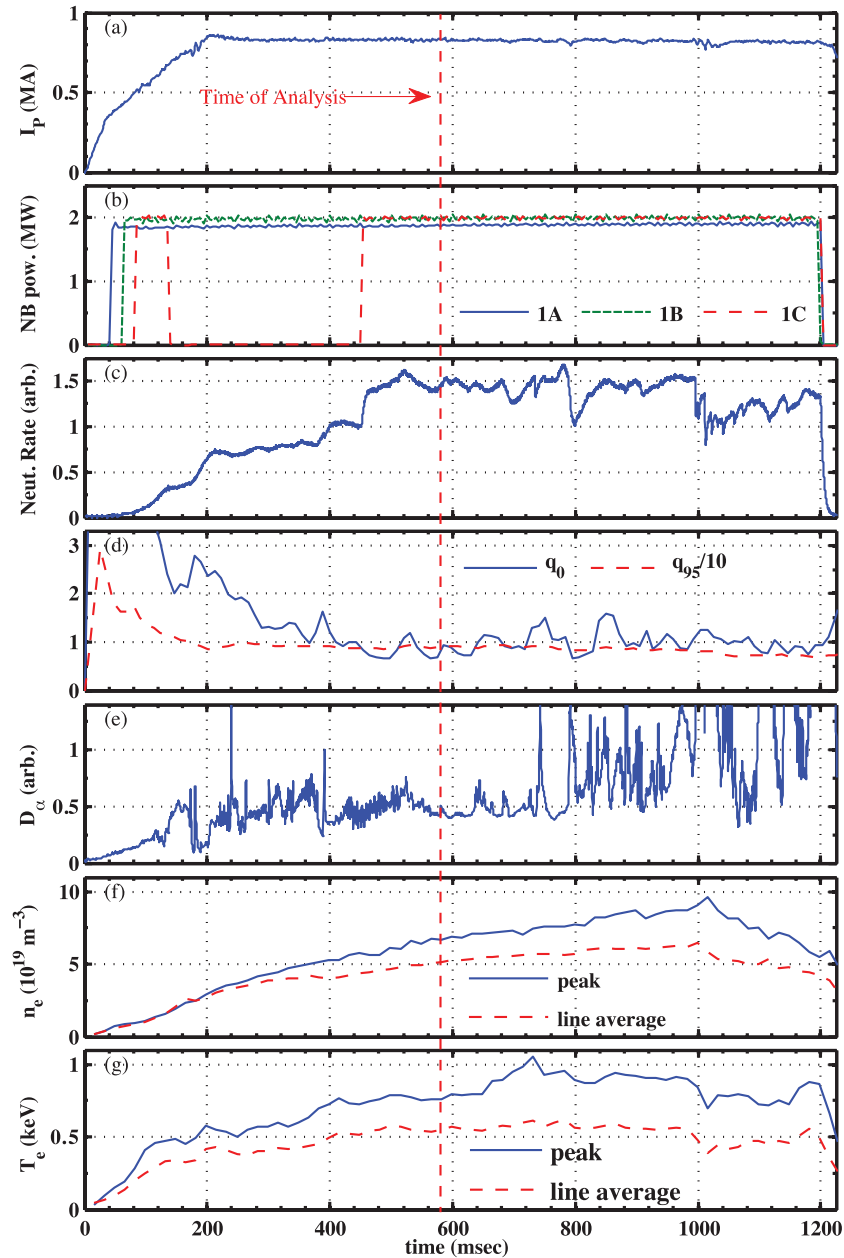
Figure 1. Plasma parameters of discharge #141398. (*a*) Plasma current (I_P); (*b*) neutral beam power (P_{NB}); (*c*) D–D fusion neutron production rate (r_{NEUT}); (*d*) plasma safety factor at magnetic axis (q_0) and 95% poloidal flux surface (q_{95}). (*e*) deuterium Balmer-α (Dα) emission; (*f*) peak and line average plasma density (n_e); (*g*) peak and line average plasma temperature (T_e).

3. Mode structure analysis technique

The global coherent nature of the CAEs and GAEs is such that each mode potentially contributes to many plasma fluctuations, including magnetic fluctuations and reflectometer measurements. In particular, NSTX features a toroidally distributed array of edge magnetic sensing coils (i.e. 'b-dot coils') that clearly detect the modes of interest (figure 3(*a*)), which have frequencies in the range $f/f_{ci0} \approx 0.17$–0.33 where $f_{ci0} = 2.4$ MHz is the ion cycltrotron frequency at the magnetic axis. Figure 3(*a*) indicates that the modes with $f < 600$ kHz are identified as GAEs, while those with $f > 600$ kHz are identified as CAEs. This identification, based on local dispersion relations and measured frequencies and toroidal mode numbers, is discussed in detail in [12]. The modes are also seen in fixed-frequency quadrature reflectometer measurements [11, 12] as illustrated in figure 3(*b*). The analysis described here exploits the global nature of a mode to isolate its contribution to each signal in the magnetic fluctuation measurements, using singular value decomposition (SVD). SVD uses the correlations of every measurement with every other to find the spatial structure of a global mode as well as the common time dependent signal of the mode. The common signal isolated from the magnetic measurements is used to extract the global mode from the reflectometer signals through their correlation with the common mode. The reflectometer measurements of each mode are then inverted using a synthetic diagnostic to obtain the density perturbation

amplitude and radial structure of the mode. The final results of this analysis are shown in figures 3(*c*) and 4. The details of this analysis are presented below.

3.1. Isolation of mode contribution to reflectometer measurements

Mode structure is determined from the fluctuating contribution, δl, to the microwave optical path length measured by each reflectometer. The path length depends on the index of refraction, N, which is a function of plasma density. It is given by the integral of N over the path traveled by the microwaves:

$$l = \int_{x_{\text{launch}}}^{x_{\text{recieve}}} N(x') \, \mathrm{d}x' \qquad (1)$$

where x_{launch} and x_{receive} are the positions of the launching and receiving antennae [23]. The modes perturb the density, and thus N, around an equilibrium value, so l is the sum of a constant plus a time dependent fluctuating part: $l = l_0 + \delta l(t)$.

The mode contribution to δl can be obtained with aid of measurements (δb) from the toroidally distributed array of magnetic sensing coils. In broad strokes, the mode contribution to the δl and δb signals is first isolated by bandpass filtering. These contributions are concentrated within a narrow spectral band around the mode frequency, as can be seen in figures 3(*a*) and (*b*), which show spectra of δb from an NSTX edge coil and δl from the 75 GHz reflectometer for the same time period. Then, the global component of the δb measurements is determined via SVD. Finally, the value of δl for the mode is taken to be the part that is coherent with the global component of δb. The steps of this analysis are discussed in detail below.

Bandpass filtering of the signal from the *i*th coil yields a signal of the form:

$$\delta b(t, \phi_i) = \delta b_{\text{mode}}(t, \phi_i) + \epsilon_i(t) \qquad (2)$$

where $\delta b_{\text{mode}}(t, \phi_i)$ is the global component and $\epsilon_i(t)$ is the contribution from local background fluctuations, as well as any noise. In keeping with the global character of the mode, $\delta b_{\text{mode}}(t, \phi_i)$ is expected to have the form:

$$\delta b_{\text{mode}}(t, \phi_i) = a_i \delta b_0(t) \cos(\omega_0 t + \theta(t) + \phi_i) \qquad (3)$$

where ω_0 is the mode angular frequency, $\delta b_0(t)$ and $\theta(t)$ are narrow band signals with bandwidth $\Delta\omega \ll \omega_0$, and a_i and ϕ_i are the relative amplitude and temporal phase shift of the *i*th coil. The global component is the same for every coil except for a phase shift and a relative amplitude, which are expected to be approximately constant over short periods of time in which the plasma equilibrium in relatively unchanging. Over longer periods of time, of course, the relative amplitudes and phase shifts might be expected to slowly change.

Another point worth noting is the consistency of this form with the assumption that global modes in a toroidal device are expected to have a sinusoidal structure in the toroidal direction due to the symmetry of the plasma equilibrium. The coils of the δb array are distributed purely in the toroidal direction, so in the absence of any systematic errors in the δb measurements, the modes should have $\phi_i = n\Phi_i$, where n is
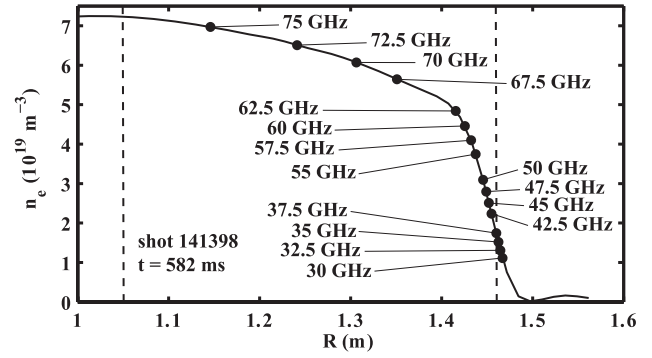

Figure 2. Plasma density profile at $t = 582$ ms, with cutoff densities marked for each channel of the reflectometer array. Vertical dashed lines indicate locations of magnetic axis ($R_0 \approx 1.05$ m) and last closed flux surface ($R_{\text{LCFS}} \approx 1.46$ m). Adapted from [11]. © IOP Publishing Ltd. All rights reserved.
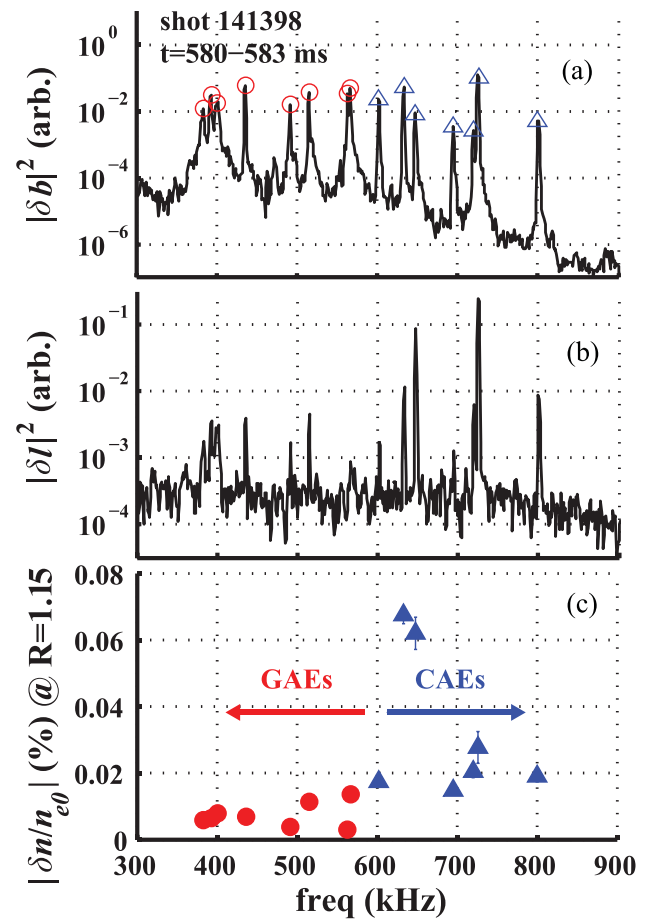

Figure 3. (*a*) δb spectrum with modes marked; (*b*) δl spectrum; (*c*) $|\delta n|$ of modes at $R = 1.15$ m (expressed as percentage of n_{e0} at R_0); In all panels, symbols $\triangle$ or o used for modes with $f >$ or < 600 kHz, respectively. Statistical uncertainties shown in (*c*). Modes with $f >$ or < 600 kHz are predominantly CAEs or GAEs, respectively [11, 12], as indicated by labeling in panel (*c*). Panel (*a*) adapted courtesy of IAEA. Figure from [12]. Copyright 2013 IAEA.

the toroidal mode number, or number of periods toroidally, and Φ_i is the toroidal location of the *i*th coil. Also, with equal sensitivities for the magnetic sensing coils, the values of a_i should all be equal. In practice, the sensitivities of the coils are not equal and there are breaks in the toroidal symmetry
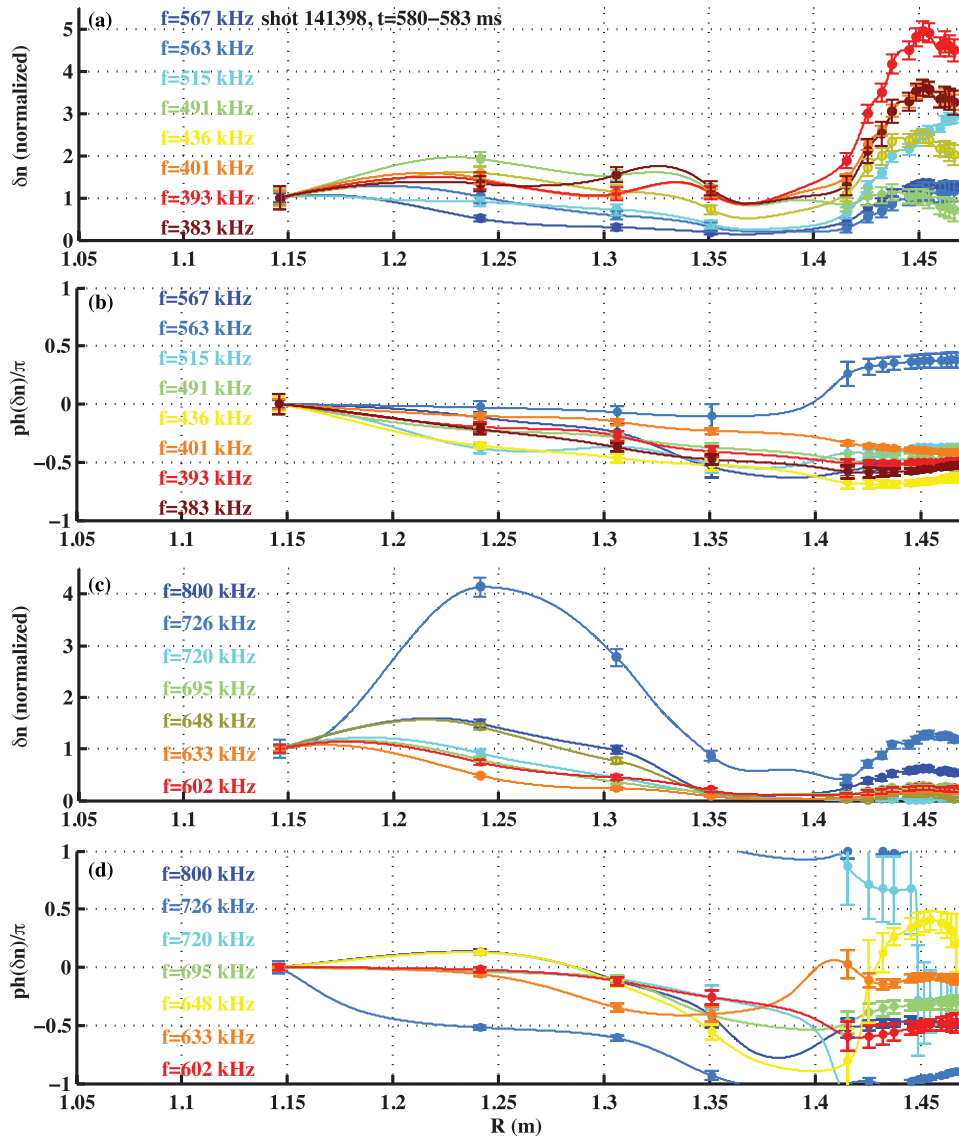
Figure 4. For modes with $f < 600\,\text{kHz}$ (GAEs): (*a*) $|\delta n|$ versus R, normalized by $|\delta n|$ at $R = 1.15\,\text{m}$ and (*b*) phase(δn)$/\pi$ versus R. For modes with $f > 600\,\text{kHz}$ (CAEs): (*c*) $|\delta n|$ versus R, normalized by $|\delta n|$ at $R = 1.15\,\text{m}$ and (*b*) phase(δn)$/\pi$ versus R. Symbols indicate reflectometer cutoffs. Statistical uncertainties shown in all panels.

of the conducting plasma facing surfaces where the coils are mounted, as well as phase shifts introduced by the electronics used to record the coil measurements. So, in the SVD analysis described below, no assumption is made regarding the values of a_i and ϕ_i. Rather, these values are determined by the SVD analysis and the toroidal mode number is then obtained by finding the mode number which best fits these values [12].

The next step is transformation of the bandpass filtered signals to obtain complex signals using what is sometimes referred to as the Hilbert Transformation. Each signal is Fourier transformed in terms of complex exponentials, $e^{i\omega t}$, and the components for $\omega \leqslant 0$ are suppressed, while the components for $\omega > 0$ are multiplied by $\sqrt{2}$ to conserved total fluctuation power. The result is subject to the inverse Fourier transformation, yielding time-dependent complex signals of the form:

$$\widehat{\delta b}(t, \phi_i) = \widehat{\delta b}_{\text{mode}}(t, \phi_i) + \widehat{\epsilon}_i(t)$$

where $\widehat{\delta b}_{\text{mode}}(t, \phi_i) = a_i \widehat{\delta b}_0(t) e^{i(\omega_0 t + \theta(t) + \phi_i)}$. (4)

The signals thus obtained are normalized to ensure $\left\langle |\delta b(t, \phi_i)|^2 \right\rangle = \left\langle \left|\widehat{\delta b}(t, \phi_i)\right|^2 \right\rangle$, where $\langle \rangle$ represents time averaging.

In this form, the set of coil signals $\widehat{\delta b}_{\text{mode}}(t, \phi_i)$ and $\widehat{\epsilon}_i(t)$ can be obtained using SVD. In the process $\widehat{\delta b}_{\text{mode}}(t, \phi_i)$ is naturally factored into a toroidal spatial structure given by

$$A_i = a_i \left|\widehat{\delta b}_0\right| e^{i\phi_i},$$

where $\left|\widehat{\delta b}_0\right| = \left\langle \left|\widehat{\delta b}_0(t)\right|^2 \right\rangle^{1/2}$ (5)

and the time-dependent global component given by the signal,

$$s_{\text{global}}(t) = \frac{\delta \widehat{b}_0(t)}{\left|\delta \widehat{b}_0\right|} e^{i(\omega_0 t + \theta(t))}. \quad (6)$$

Singular value decomposition solves the problem of factoring a spatial array of magnetic fluctuation signals by finding $A_i \forall i$ and $s_{\text{global}}(t) \, \forall t$ to minimize the squared error function

$$\chi^2 = \sum_i \left\langle \left| \delta \widehat{b}(t, \phi_i) - A_i s_{\text{global}}(t) \right|^2 \right\rangle. \quad (7)$$

This minimization problem can be rearranged into an eigenvector problem for the values of A_i,

$$\mathbf{B}\boldsymbol{\alpha} = \lambda \boldsymbol{\alpha}$$

where $B_{ij} = \left\langle \delta \widehat{b}^*(t, \phi_i) \delta \widehat{b}(t, \phi_j) \right\rangle$ and $\|\boldsymbol{\alpha}\| = 1$. $\quad (8)$

Each eigenvector and its associated eigenvalue, $\boldsymbol{\alpha}$ and λ, can be used to construct values, $A_i = \lambda^{\frac{1}{2}} \alpha_i$, that correspond to a local minimum of χ^2. The global minimum is obtained using the eigenvector, $\boldsymbol{\alpha}_{\text{max}}$, with the largest eigenvalue, λ_{max}. The eigenvectors of $\mathbf{B}$ are orthogonal, so the global mode signal can be constructed from λ_{max} and $\boldsymbol{\alpha}_{\text{max}}$

$$s_{\text{global}}(t) = \lambda_{\text{max}}^{-\frac{1}{2}} \sum_i \alpha_{\text{max},i}^* \delta \widehat{b}(t, \phi_i). \quad (9)$$

Because the magnetic signals used in this analysis are narrowband with a common frequency, the largest eigenvalue is typically much larger than the others. If the other, smaller eigenvalues are comparable to each other in magnitude, then $|\langle \widehat{\epsilon}_i^*(t) \widehat{\epsilon}_j(t) \rangle|$ is typically much larger for $i = j$ than $i \neq j$ (i.e. $\widehat{\epsilon}(t, \phi_i) = \widehat{\epsilon}_i(t)$ has a short spatial correlation length), as expected for non-global noise or background fluctuations. If, however, the 2nd largest eigenvalue is substantially larger than the others, this suggests there are actually at least two distinct global modes contributing to the bandpass filtered signals and further analysis, beyond the scope of this article, may be necessary to decompose the signals into the independent global modes. Of course, if the 2nd eigenvalue is much smaller than the largest, then $s_{\text{global}}(t)$ constructed using λ_{max} and $\boldsymbol{\alpha}_{\text{max}}$ gives a reasonable approximation of the dominant global mode even in this case.

The complex path length fluctuation for the mode, δl_{mode}, is then determined by bandpass filtering and transforming $\delta l(t)$ to a complex signal $\widehat{\delta l}(t)$ and isolating the part that is coherent with $s_{\text{global}}(t)$. In keeping with the global nature of the mode, the signal $\widehat{\delta l}(t)$ is assumed to be of the form:

$$\widehat{\delta l}(t) = \widehat{\delta l}_{\text{mode}}(t) + \widehat{\epsilon}_{\delta l}(t) = A_{\delta l} s_{\text{global}}(t) + \widehat{\epsilon}_{\delta l}(t) \quad (10)$$

where $A_{\delta l} = a_{\delta l} e^{i\phi_{\delta l}}$ is the complex amplitude of $\widehat{\delta l}_{\text{mode}}(t)$ and $\epsilon_{\delta l}(t)$ is a contribution from background fluctuations that are not global, as well as any noise. The complex amplitude of the mode path length fluctuations is then simply obtained by:

$$A_{\delta l} = \left\langle \widehat{\delta l}(t) s_{\text{global}}^*(t) \right\rangle. \quad (11)$$

This correlation technique for determination of mode contribution to δl has an advantage over simple bandpass filtering.

The δl signals typically have relatively large contributions from background fluctuations which are captured by the bandpass filtering along with the contribution from the mode. The δb, in contrast, have relatively small background fluctuations. This is illustrated in figures 3(a) and (b), where the peak-to-background ratio of the δl spectrum is much smaller than for δb. This correlation technique filters out the residual contribution of the background fluctuations to the bandpass filtered δl, leaving only the contribution from the mode.

Since finite length time records are used and limited bandwidth is imposed in separating $s_{\text{global}}(t)$ from $\widehat{\epsilon}_i(t)$, and $\widehat{\delta l}_{\text{mode}}(t)$ from $\widehat{\epsilon}_{\delta l}(t)$, the separation is not expected to be perfect and $A_{\delta l}$ will have a statistical uncertainty, $u(A_{\delta l})$, which can in principle be estimated from $\left\langle |\widehat{\epsilon}_i|^2 \right\rangle$ and $\left\langle |\widehat{\epsilon}_{\delta l}|^2 \right\rangle$. In practice, the contribution from $\left\langle |\widehat{\epsilon}_i|^2 \right\rangle$ is neglected since, as can be seen in figure 3(a), the modes have large peak-to-background ratios in the magnetic spectrum, so $\left\langle |\widehat{\epsilon}_i|^2 \right\rangle$ is relatively small. The uncertainty is then given approximately by $|u(A_{\delta l})|^2 \approx \left\langle |\widehat{\epsilon}_{\delta l}|^2 \right\rangle / N_f$, where $N_f = \tau \Delta \omega$—the number of frequencies within bandwidth $\Delta \omega$ for records of length τ—is effectively the number of independent measurements used in determining $A_{\delta l}$. As an example, these uncertainties are illustrated for the $f = 800$ kHz mode in figure 6(a).

3.2. Inversion of mode path length fluctuations

The measurements of path length fluctuations (δl) from the reflectometers (defined in previous section) can be thought of as samples at particular frequencies of a function of microwave frequency (ω), the equilibrium density profile (n_e) and the density perturbation (δn). Using these measurements and knowledge of n_e, this function, $\delta l(\omega, n_e, \delta n)$, can be inverted with the aid of a synthetic diagnostic to obtain δn. The path of the microwaves is approximately along a major radial chord in the plasma midplane for all channels of the array, so inversion of the measurements yields $\delta n(R)$, the density perturbation as a function of major radius in the plasma midplane from the plasma edge to the cutoff location of the highest frequency channel.

Using the techniques described in the previous section, the contribution of a mode to the array of δl measurements can factored in terms an array of complex amplitudes, one for each reflectometer, and a complex global time-dependent signal common to all the reflectometers. A complex density perturbation as a function of R can be obtained for the mode by treating the real and imaginary parts of the complex δl amplitudes separately. Combining the complex density perturbation with the global signal and taking the real part gives $\delta n(R, t)$. The amplitude of the complex density perturbation determines the amplitude of $\delta n(R, t)$, while the phase imposes a temporal delay in $\delta n(R, t)$ that varies with R.

The inversion (for either the real or imaginary parts of the complex δl amplitudes) is performed by constructing a model δn using a linear combination of basis perturbations:
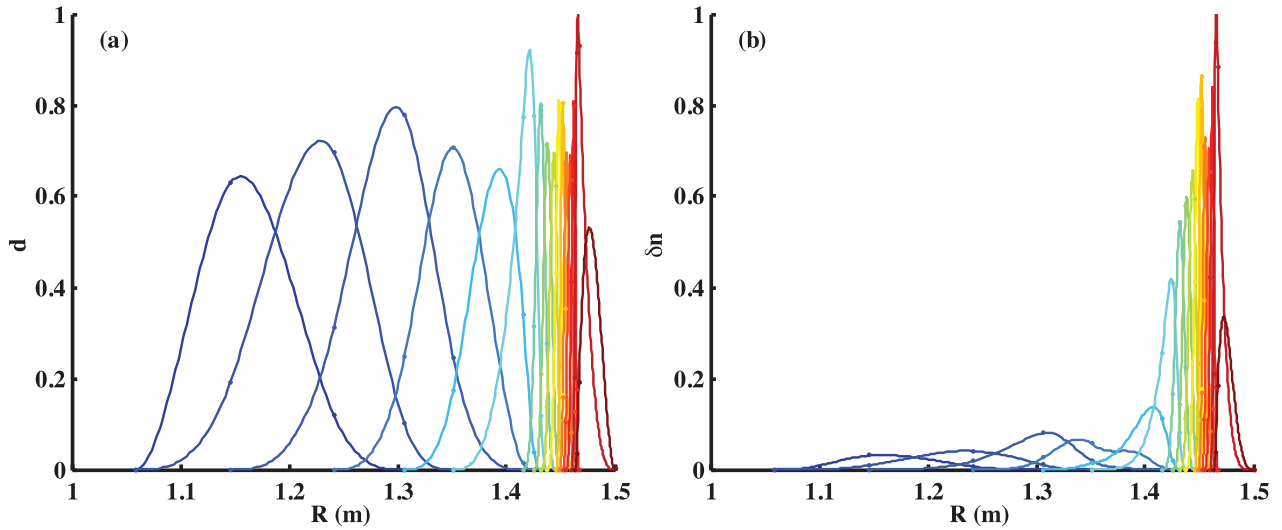
Figure 5. Basis (*a*) displacement perturbations and (*b*) density perturbations.

$$\delta n (R) = \sum_i c_i \delta n_i (R) \tag{12}$$

Coefficients are chosen that best reproduce the set of δl. A synthetic reflectometer diagnostic based on a 1D model of microwave propagation is used to calculate the expected value of δl for each reflectometer assuming the model δn, and the coefficients are then adjusted to achieve values that are a good fit to the measured δl.

For a perturbed density profile $n_e (R) = n_e (R) + \delta n (R)$ and microwave frequency ω, the synthetic diagnostic assumes path length $l (\omega, n_e)$ to be given by an integral over the microwave path [23]:

$$l (\omega, n_e (R, t)) = 2 \int_{R_{\text{antenna}}}^{R_{\text{cutoff}}(\omega, n_e)} N (\omega, n_e (R, t)) \, dR + \frac{\pi}{2} \frac{c}{\omega} \tag{13}$$

where $N (\omega, n_e)$ is the index of refraction and $R_{\text{cutoff}} (\omega, n_e)$ is defined by the condition $N = 0$. For the measurements in [11, 12], O-mode polarization is used, so $N (\omega, n_e) = \sqrt{1 - \omega_p^2 / \omega^2}$, where $\omega_p^2 = e^2 n_e / \epsilon_0 m_e$ is the plasma frequency.

In principal, the calculated δl can depend nonlinearly on the coefficients of the model δn. However, the measured values of δl for the case considered here are small enough that δl can be accurately calculated from a linear combination of values for the individual basis perturbations. This reduces the inversion procedure to solving a linear system of equations.

For the ith basis function δn_i, the path length fluctuation δl_i is a function of the equilibrium density profile n_e and microwave frequency ω, and is calculated using relation:

$$\delta l_i (\omega, n_e (R)) = \delta l (\omega, n_e (R), \delta n_i (R))$$
$$= \frac{1}{2} (l (\omega, n_e + \delta n_i) - l (\omega, n_e - \delta n_i)) \tag{14}$$

where the right hand side is evaluated using a small amplitude for δn_i so that δl_i is approximately linear in the amplitude. The integrals are evaluated using the Matlab *quadgk* routine, which implements adaptive quadrature integration based on a Gauss–Kronrod pair (15th order Kronrod and 7th order Gauss formulas) [24].

Taking into account the construction of the model δn (equation (12)), the path perturbation for the jth reflectometer $\delta l (\omega_j, n_e, \delta n)$ is given by:

$$\delta l (\omega_j, n_e (R), \delta n (R)) = \sum_i c_i \delta l_i (\omega_j, n_e (R)). \tag{15}$$

For the purposes of the numerical integration, the equilibrium density function, n_e is implemented with a cubic-spline interpolating the measurements from MPTS (figure 2).

To simplify interpretation of δn, the basis density perturbations, δn_i, are derived by convection of the equilibrium density profile using a basis set of major radial displacement perturbations d_i:

$$\delta n_i (R) = -d_i (R) \nabla n_e (R). \tag{16}$$

With this approach, after the coefficients c_i have been determined from the measurements it is a simple matter to reconstruct the displacement profile of the equilibrium density profile that produces δn:

$$d (R) = \sum_i c_i d_i (R). \tag{17}$$

It should be noted that d is a displacement of the equilibrium density contours in the major radial direction. In general, d is not equal to the plasma fluid displacement in the major radial direction, $\xi \cdot \hat{R}$, (e.g. the $E \times B$ displacement) except when the density perturbation is incompressible and the density gradient scale length is much shorter than the major radius. This is clearly not the case for CAEs. However, for GAEs in the edge region where the density gradient is large, $d (R)$ is potentially a useful approximation of $\xi \cdot \hat{R}$. As discussed in section 4, fluid compression contributes to δn, and thus to d. This is true even for shear modes, where geodesic compression results from fluid displacement along the gradient of B_0 [25, 26].

The set of basis displacement perturbations used are cubic (i.e. '4th order') normalized B-splines [27] with knots at the magnetic axis ($R_0 \approx 1.05$ m), the cutoff locations of each channel (see figure 2) and the plasma edge ($R = 1.5$ m).

Figure 5(*a*) shows the basis displacement perturbations and figure 5(*b*) shows the derived basis density perturbations used in constructing δn. Cubic splines can be fully specified by providing values at the knots and the slope at each endpoint. For purposes of this inversion technique, only a subset of the cubic normalized B-splines for the given knots is actually used. The subset is chosen to ensure by construction that $\delta n = 0$ and $\mathrm{d}(\delta n)/\mathrm{d}R = 0$ at the endpoints (R_0 and $R = 1.5$ m). These conditions are chosen because they are easily implemented and they allow the slope and value of δn at each of cutoff locations for the array to vary relatively freely when fitting the measurements. However, while these conditions serve as a useful starting point for development of the inversion technique, they merit further consideration in future work. Although the choice to enforce $\delta n = 0$ at $R = 1.5$ m is relatively easy to motivate, the physical motivation for the other boundary conditions warrants further consideration.

The inversion is sensitive to short scale structure in $\delta l\,(\omega, n_e, \delta n)$. ($\delta l\,(\omega, n_e, \delta n)$ can be treated as a function of R for a given n_e profile by mapping ω to R through the relation $R = R_{\mathrm{cutoff}}\,(\omega, n_e)$.) Small random errors in the measured δl, which can introduce substantial unphysical short scale structure, can translate to large errors in the reconstructed δn. This concern is addressed by smoothing the measured δl prior to the reconstruction as much as justifiable taking into account the statistical uncertainties of the measurements.

The smoothing is performed by treating the set of $\delta l\,(\delta n, n_e, \omega_j)$ versus $R_{\mathrm{cutoff}}\,(n_e, \omega_j)$ as measurements of a function of R and finding a best-fit cubic spline while imposing a penalty for excessive curvature [28]. In particular, a cubic spline is chosen to have minimum curvature subject to the constraint that the r.m.s. uncertainty-weighted difference between fitted and measured δl is less than ~1. The set of knots and boundary conditions for the smoothing spline are different from those used for the cutoff displacement. The knots include only the cutoff locations and the plasma edge, $R = 1.5$ m. The slope at the plasma edge, $R = 1.5$ m, is constrained to be 0, motivated by the assumption the plasma edge is displaced rigidly by the mode. The slope at the innermost knot and the value of the spline at the plasma edge, $R = 1.5$ m, are chosen to minimize overall curvature of the spline. (These values implicitly depend on the values of the spline at the other knot points.)

It is worth noting that smoothing can also be physically motivated by the observation that for CAEs, which are compressional Alfvén waves confined in the plasma, short scale structure should lead to high frequency. While this consideration does not inform the smoothing method employed here, in principle it could, but that is left to future work.

When the values of δl from the smoothed spline are inverted, a much smoother δn results. As an example, the results of the smoothing for the $f = 800$ kHz mode are illustrated in figure 6. Figure 6(*a*) shows the raw measured and smoothed δl (δl is shown in terms of effective displacement, $d_{\mathrm{eff}} = \frac{\delta l}{2}$). The contrast in the results of inverting the smoothed and unsmoothed δl is illustrated in figure 6(*b*). Notably, δn from the unsmoothed δl exhibits large amplitude oscillations in the plasma edge ($R > 1.35$ m) that are absent in δn from
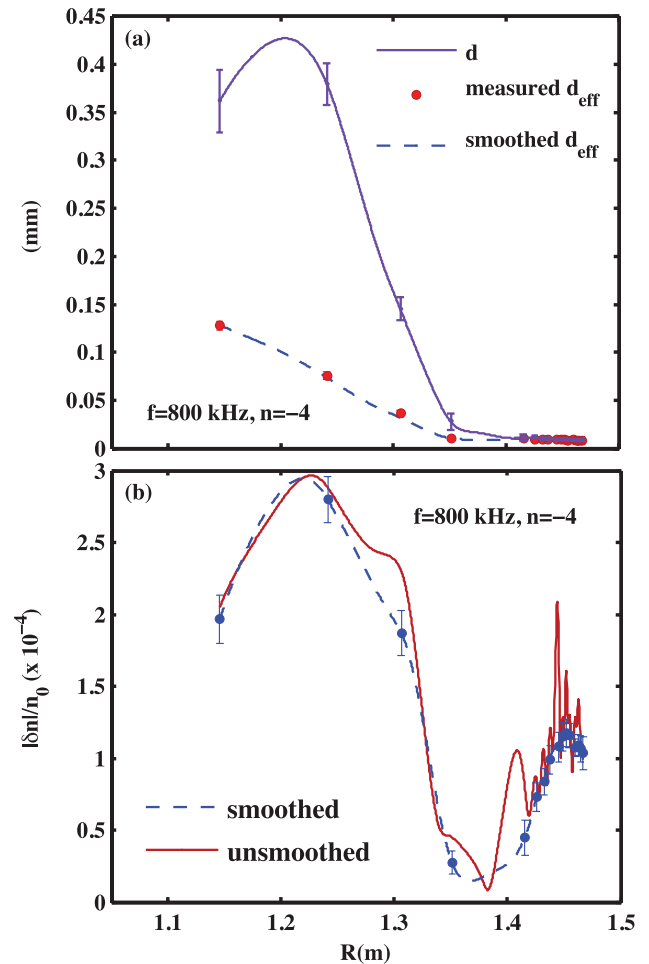

Figure 6. (*a*) Measured and smoothed d_{eff} (i.e. $\delta l/2$) for the $f = 800$ kHz mode and, for comparison, d obtained from smoothed δl; statistical uncertainties for the measured d_{eff} are smaller than the plot symbols; (*b*) δn from inverting the smoothed and unsmoothed δl, normalized by n_{e0} at the magnetic axis.

the smoothed δl. While it might be natural to suspect that the smoothing procedure is suppressing real structure in the resulting δn, it is not actually possible to know whether that structure is real, given the measurement uncertainties. This is clearly illustrated by noting that despite the large edge δn differences, the smoothed δl in the edge deviates from each δl measurement by less than its statistical uncertainty.

For comparison with d_{eff}, figure 6(*a*) also shows the cutoff displacement, d, obtained from the inversion for the $f = 800$ kHz mode. As discussed in [11, 12], d_{eff} can serve as an estimate for cutoff displacement, albeit a cruder one than d. The value of d_{eff} estimates the cutoff displacmement using the 'mirror approximation', in which δl is assumed to be due to motion of the cutoff caused by δn in the vicinity of the cutoff. This approximation is most accurate in the limit of long radial wavelength, when the mode rigidly displaces the plasma radially. Note that d is much larger than d_{eff}. This has potentially significant implications which are discussed below.

Statistical uncertainties for the measured δl (calculated as described above in section 3.1) are propagated to obtain statistical uncertainties (not shown) for the smoothed δl, making the reasonable assumption that the background fluctuations

measured by each channel are uncorrelated. These uncertainties are then propagated to obtain uncertainties for δn and d. Examples are illustrated for the $f = 800\,\text{kHz}$ mode in figures 6(*a*) and (*b*). Figure 3(*c*) shows uncertainties in the amplitude of δn for all modes at the innermost cutoff, $R = 1.15$ m. For many modes, the uncertainties are smaller than the plot symbols.

3.3. Results of mode isolation and inversion

The results of the inversion for the modes seen in figures 3(*a*) and (*b*) are shown in figures 3(*c*) and 4. Figure 3(*a*) shows the spectrum of edge magnetic fluctuations, marked to show 15 modes found [11, 12] to be predominantly GAEs for $f < 600\,\text{kHz}$ and CAEs for $f > 600\,\text{kHz}$. Figure 3(*b*) shows the δl spectrum of the highest frequency reflectometer, with corresponding peaks for the modes. Figure 3(*c*) shows $|\delta n|$ at $R = 1.15$ m, normalized by equilibrium density (n_{e0}) at the magnetic axis. Figures 4(*a*) and (*c*) show $|\delta n|$ versus R for each mode normalized using $|\delta n|$ at $R = 1.15$ m to facilitate comparison of structures. Figures 4(*b*) and (*d*) show phase $(\delta n)/\pi$ versus R for each mode, where phase (δn) is the temporal phase of the $\delta n(R)$ relative to $\delta n(R = 1.15\,\text{m})$. Figures 4(*a*) and (*b*) show modes with $f < 600\,\text{kHz}$ (GAEs), while figures 4(*c*) and (*d*) show modes with $f > 600\,\text{kHz}$ (CAEs). (The magnetic axis is $R_0 \approx 1.05$ m and the plasma edge is $R = 1.5$ m). (Note that [12] reported a cutoff location for the deepest channel of $R = 1.16$ m, based on a density profile using unsmoothed MPTS measurements. The cutoff locations in figure 4 are based on the smoothed profile shown in figure 2.)

The CAEs tend to have δn with larger amplitude in the plasma core than in the edge, while the opposite tends to be true for the GAEs. The temporal phase of δn varies significantly from core to edge (as much as π) for most modes. The modes with $f > 600\,\text{kHz}$ tend to feature distinct $|\delta n|$ peaks in both the core and edge of the plasma, with the latter being much lower amplitude. In contrast, the modes with $f < 600\,\text{kHz}$ tend to have low amplitude, relatively flat core $|\delta n|$ profiles with large amplitude peaks in the edge. Edge localized peaks are seen in the structure of all modes. The peaks occur in the pedestal, likely resulting from the structure of the equilibrium density profile, which has steep gradient in the pedestal region ($R \approx 1.41$ m–1.5 m). Even a small radial plasma displacement in the pedestal can cause a large density perturbation there.

As noted above, the inversion technique yields not just δn, but also density contour radial displacement, $d = -\delta n/\nabla n_e$. Table 1 lists values of $\delta n/n_{e0}$ and d for the modes shown in figure 3(*c*), along with the effective displacement, d_{eff} (i.e. $\delta l/2$) (from [12]) for comparison, at $R = 1.15$ m. (Note, the value of n_{e0} is given by the maximum of the the density profile, $n_e(R)$, in figure 2: $n_{e0} = 7.25 \times 10^{19}$ m^{-3}.) Recall from the previous section that d_{eff} is an estimate of the cutoff displacement using the mirror approximation. Table 1 also shows the measured mode frequencies and toroidal mode numbers of the modes (also from [12]) for reference. As can be seen from table 1, the displacements from the inversion are larger than d_{eff} by a factor of ~2–4. This is also illustrated graphically in

Table 1. Measured frequency, toroidal mode number (n) (see figure 2, [12]), density fluctuation ($\delta n/n_{e0}$), displacement (d) and effective displacement (d_{eff}) (see figure 1(*b*), [12]) of modes shown in figure 3(*c*).

Freq. (kHz)	n	$\delta n/n_{e0}$ (10^{-4})	d (mm)	d_{eff} (mm)
383	−8	0.58	0.11	0.04
393	−7	0.65	0.12	0.05
401	−8	0.78	0.15	0.06
436	−7	0.70	0.13	0.05
491	−8	0.37	0.07	0.03
515	−7	1.13	0.22	0.06
563	−6	0.30	0.06	0.03
567	−8	1.37	0.26	0.06
602	−5	1.74	0.33	0.09
633	−4	6.75	1.28	0.30
648	−1	6.20	1.18	0.40
695	−5	1.48	0.28	0.08
720	0	2.05	0.39	0.12
726	−3	2.77	0.53	0.30
800	−4	1.91	0.36	0.13

figure 7, which shows the ratio, d/d_{eff} for each of the modes. The values of d are likely larger than d_{eff} because δn tends to be small between the edge and the core for all the modes, and while d_{eff} is determined in part by the motion of the cutoff, there is also contribution from the weighted average of δn along the path, where the weighting deprecates the significance of the edge peak.

4. Discussion

The values of δn (or d) allow for estimates of plasma fluid displacement (ξ)—which can be related to the electromagnetic perturbation associated with the mode—using the continuity equation:

$$\delta n/n_e = -\nabla \cdot \xi - \xi \cdot \nabla \ln (n_e).\qquad(18)$$

The electromagnetic perturbation is necessary for a variety of purposes, including, for instance, to simulate the effects of the modes on electron orbits and the resulting electron thermal transport (as in [7]). With physically reasonable assumptions typical for global magnetohydrodynamic waves, it can be shown that:

$$\nabla \cdot \xi = -\delta b_\parallel/B - 2\xi \cdot \nabla \ln (B) - \frac{1}{2}\beta\xi \cdot \nabla \ln (p)\quad(19)$$

where $\beta = p/(B^2/2\mu_0)$. The term $2\xi \cdot \nabla \ln (B)$ is sometimes referred to as the geodesic [25] or ideal MHD [26] compression effect. In particular, equation (19) holds true if the equilibrium magnetic field is in force balance with an isotropic plasma pressure ($\mathbf{J} \times \mathbf{B} - \nabla p = 0$), plasma fluid displacement is due to $E \times B$ motion ($\xi = \delta\mathbf{E} \times \mathbf{B}/(-i\omega B^2)$), the electric field perturbation has no parallel component ($\delta\mathbf{E} \cdot \mathbf{B} = 0$) and the time derivative of $\delta\mathbf{E}$ can be neglected in Ampère's Law ($\nabla \times \mathbf{B} = \mu_0\mathbf{J}$). It can be shown from equations (18) and (19)
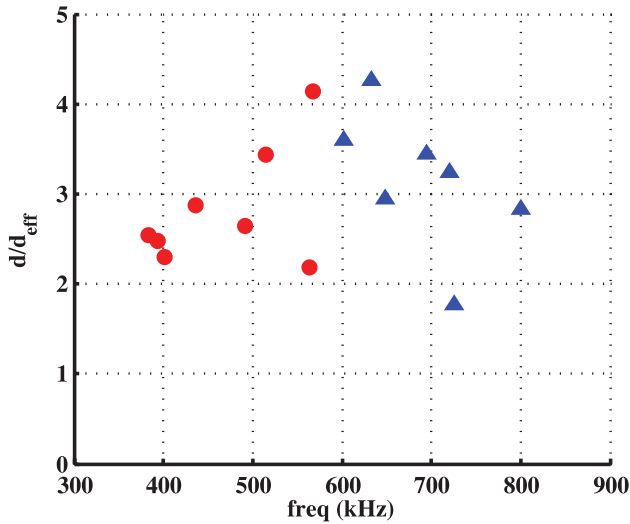
Figure 7. Ratio of density contour displacement from inversion, d, to effective displacement, d_{eff}, at $R = 1.15$ m. Symbols Δ or o used for modes identified as CAEs or GAEs respectively.

that, assuming $\delta b_{\parallel}/B$ is negligible, the density contour displacement (d) is related to $\xi_R = \boldsymbol{\xi} \cdot \widehat{\mathbf{R}}$ in the plasma midplane by:

$$d = \left(1 - \frac{2\partial \ln\left(B\right)/\partial R + \frac{1}{2}\beta\partial\ln\left(p\right)/\partial R}{\partial\ln\left(n_{\mathrm{e}}\right)/\partial R}\right)\xi_R. \quad (20)$$

The various proportionality factors from the equilibrium profiles in equations (18) and (19) that relate the plasma fluid displacement ($\boldsymbol{\xi}$) to the density perturbation ($\delta n/n_{\mathrm{e}}$) are shown in figure 8. The total of all the proportionality factors is also shown. The profiles of p and β used in figure 8 are determined from EFIT equilibrium reconstruction [19, 20] taking into account measurements of electron density and temperature from MPTS and ion density and temperature from charge exchange recombination spectroscopy [29]. The reconstruction also allows for fast-ion pressure, loosely constrained by fast-ion pressure from TRANSP modeling [20].

It should be noted that for high aspect ratio tokamaks, where $B \propto 1/R$ and $\beta \ll 1$, further simplification would be possible, leading to [26]:

$$\delta n/n_{\mathrm{e}} \approx \widetilde{b}_{\parallel}/B - 2\boldsymbol{\xi}\cdot\widehat{\mathbf{R}}/R - \boldsymbol{\xi}\cdot\nabla\ln\left(n_{\mathrm{e}}\right). \quad (21)$$

However, neither of these approximations is valid for the discharge under consideration. The poloidal magnetic field can be comparable to the toroidal magnetic near the plasma edge, so $B \not\propto 1/R$. Also, β is large ($\beta \sim 70\%$ at the magnetic axis) and $|(\beta/2)\nabla\ln\left(p\right)| \sim |\nabla\ln\left(n_{\mathrm{e}}\right)|$ for most of the plasma, as can be seen in figure 8.

Another assumption that must be considered carefully for the high frequency modes under consideration is that the plasma fluid displacement is purely from $E \times B$ motion. The modes have frequencies in the range $f/f_{\mathrm{ci0}} \approx 0.17$–$0.33$, so finite frequency effects that are typically neglected in the approximation $\boldsymbol{\xi} = \delta\mathbf{E} \times \mathbf{B}_0/\left(-i\omega B_0^2\right)$ may be important. Specifically, the fluid displacment will have a contribution from polarization drift that is smaller than the $E \times B$
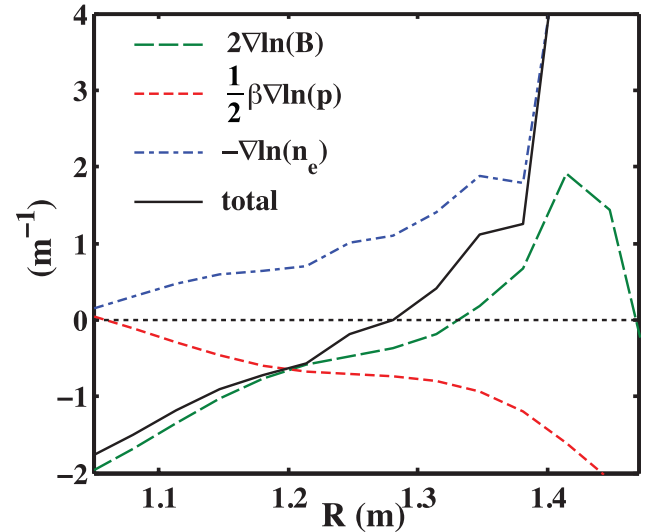

Figure 8. Dashed lines show various proportionality factors in equations (18) and (19) from equilibrium profiles relating plasma fluid displacement ($\boldsymbol{\xi}$) to density perturbation ($\delta n/n_{\mathrm{e}}$). Solid line shows total of all factors.

displacement by a factor of $\omega/\omega_{\mathrm{ci}}$. This extra component will contribute to $\nabla \cdot \boldsymbol{\xi}$ fundamentally differently. For the purposes here of evaluating mode impacts on heating and energy transport, this extra component will be neglected since the correction to $\boldsymbol{\xi}$ is less than 30%, which is unlikely to change the fundamental conclusions, as will be seen.

It is interesting to note that that for a peaked density and pressure profile, and for B decreasing with R, the $\nabla\ln\left(n_{\mathrm{e}}\right)$ term in equation (18) competes with other gradient terms entering equation (18) through the $\nabla \cdot \boldsymbol{\xi}$ term. For modes with negligible $\delta b_{\parallel}/B$, $E \times B$ displacement should cause vanishingly small $\delta n/n_{\mathrm{e}}$ at some R in the midplane on the low magnetic field side of the plasma. For this discharge, that occurs at $R = 1.28$ m (figure 8). Many of the GAE mode structures in figure 4(*a*) do not show a strong amplitude minimum, while others show a minimum around $R \sim 1.35$ m–1.4 m. This suggests that these modes may have significant $\delta b_{\parallel}/B$ around $R \sim 1.3$–1.4 m, or that the polarization drift contribution to $\boldsymbol{\xi}$ is not negligible there, causing the minimum to not appear or to shift location. GAEs in simulations [10] of the Hybrid MHD (HYM) code show significant $\delta b_{\parallel}/B$ on the low field side, so this is not unexpected.

One application of the inversion results shown in table 1 is to make an improved comparison of experimental GAE amplitudes with the threshold predicted by [7] to explain the anomalous electron thermal transport typical of discharges like the one in which the inverted reflectometer measurements were obtained. A previous attempt at the comparison was made in [12], using the values of d_{eff} for GAEs ($f < 600$ kHz) shown in table 1. Using the values of $\delta n/n_{\mathrm{e0}}$ from table 1 instead, along with equations (18) and (19), it is possible to make a more accurate comparison with the predicted threshold. At $R = 1.15$ m, the measurement location for the values in table 1, the proportionality factors for equations (18) and (19) that are shown in figure 8 are $-\nabla\ln\left(n_{\mathrm{e}}\right) = 0.6$ m^{-1}, $(\beta/2)\nabla\ln\left(p\right) = -0.5$ m^{-1}, and $2\nabla\ln\left(B\right) = -1$ m^{-1}, for a total of -0.9 m^{-1}. Also, it is worth noting that the density at $R = 1.15$ m is $n_{\mathrm{e}} = 7.0 \times 10^{19}$ m^{-3}, while the values of δn

in table 1 are normalized to the density at the magnetic axis, $n_{e0} = 7.25 \times 10^{19}$ m^{-3}.

Reference [7] presents modeling of electron drift orbits in the presence of multiple modes showing that at sufficient amplitude, the orbits are stochastized, leading to enhanced electron thermal diffusivity (χ_e). The threshold amplitude is expressed in terms of the parameter $\alpha = \delta A_\parallel / B_0 R_0$, where $\delta A_\parallel$ is the parallel component of the perturbed vector potential. To explain the anomalous electron thermal transport, at least 16 modes are required, each with an amplitude of $\alpha_0 \geqslant 4 \times 10^{-4}$, for a total amplitude of $> 6 \times 10^{-3}$. In [12], values of α were calculated from the values of d_{eff} for each GAE using the measured frequencies and toroidal mode numbers in table 1, and the GAE dispersion relation. This yielded a total amplitude of 3.4×10^{-4}, which falls well below the threshold. (Note that [12] mistakenly compared the *total* experimental GAE amplitude to the predicted *per-mode* threshold $\alpha_0 = 4 \times 10^{-4}$, incorrectly concluding that the modes reached the predicted threshold.) Using the values of $\delta n / n_{e0}$ from table 1 instead of d_{eff} to calculate α for each mode, and assuming $\widetilde{b}_\parallel / B$ is negligible for the GAEs, which are shear-like eigenmodes, yields a total GAE amplitude of 6×10^{-4}. This is ~75% larger, but still well below the threshold, so the GAEs amplitudes are not large enough to explain the transport. Note that the polarization drift contribution to ξ is neglected as discussed above because the total GAE amplitude is a factor of 10 below the threshold. Accounting for it would be unlikely to change the conclusion. The modeling in [7] showed the thermal diffusivity to have a strong nonlinear dependence on amplitude ($\chi_e \propto \alpha^c$, $c = 3 - 6$), so the factor of ~10 difference between the experimental amplitude and the threshold makes an enormous difference in the expected diffusivity. It should also be noted that as discussed in [12], the number of GAEs is also well below the predicted threshold for causing the transport.

The contribution of the CAEs ($f > 600$ kHz) was not included in the comparison above since the theory for the diffusion enhancement in [7] has not yet been extended to include modes of compressional polarization. However, it is worth considering how those modes would contribute if they were, in fact, GAEs (i.e. if they had been misidentified in [11, 12]). Using the values of $\delta n / n_{e0}$ for all modes in table 1 to calculate α yields a total amplitude of 9×10^{-4}. This is not that much larger than for just the modes with $f < 600$ kHz, so the total mode amplitude would still fall well below predicted threshold for causing the transport, even though the total number of modes would be high enough. Notably, the values of $\delta n / n_{e0}$ for the modes with $f > 600$ kHz tend to be larger than those with $f < 600$ kHz. However, this is offset in the calculated values of α for these modes by the dependence of α on poloidal mode number (m), which is $\alpha \propto m^{-1}$. The higher frequencies and lower toroidal mode numbers of these modes leads to higher values of m inferred from the GAE dispersion relation. While the modes with $f < 600$ kHz have $|m| \sim 1/2 - 2\frac{1}{2}$, as indicated in [12], the modes with $f > 600$ kHz have $|m| \sim 4-11$.

The inversion results also have implications for another important hypothesized core energy transport mechanism, coupling of CAEs to kinetic Alfvén waves (KAW) [9, 10]. Simulations of CAEs using the HYM code showed significant energy electromagnetically transported across the plasma by the modes. Specifically, the simulations showed that CAEs take energy from the core localized beam ions that excite them (thus diverting energy from core heating) and deposit the energy in the outer part of the plasma via coupling or mode conversion to KAWs, which are highly dissipative. The energy transported is proportional to the square of the mode amplitude. Using the experimental values of d_{eff} from [12] to set the amplitude of the modes, the energy transported by the CAEs in the experiment was estimated in [9, 10]. (The values of d_{eff} from [12] are also shown in table 1, where CAEs are modes with $f > 600$ kHz.) Specifically, the values of d_{eff} were used to set the amplitude of the simulated plasma displacement perturbation and all other associated mode perturbations were scaled accordingly, yielding $\delta b_\parallel / B_0 \sim 0.9$–$3.4 \times 10^{-3}$. Since CAEs are compressional and the profile gradients in the core are shallow, it is clear from equations (18) and (19) that the approximation $\delta b_\parallel / B_0 = \delta n / n_e$ can be used instead. Using $\delta n / n_{e0}$ from table 1 and $n_{e0} / n_e = 1.04$, it can be seen that $\delta b_\parallel / B_0$ in the experiment is actually much smaller (e.g. at $f = 648$ kHz, $\delta n / n_e = (\delta n / n_{e0})(n_{e0}/n_e) = (6.2 \times 10^{-4})(1.04) = 6.5 \times 10^{-4} \ll 3.4 \times 10^{-3}$) suggesting that the energy transport by CAEs is significantly over-predicted in [9, 10]. For instance, the simulations showed that a nonlinearly saturated $n = 4$ CAE with $\delta b_\parallel / B_0 \sim 6.6 \times 10^{-3}$ would lose 1.2 MW through the coupling to KAWs. Assuming that the lost power scales simply as $\delta b_\parallel^2$, as is done in [10], and that the scaling is the same for all CAEs, the CAEs in table 1 would collectively lose ~0.03 MW. It is also worth noting that the experimental amplitudes are much smaller than the CAE saturation amplitude in the nonlinear simulations discussed in [9, 10], highlighting a potentially fruitful area for further development of the physics model of HYM.

Another area in which the inversion results can be exploited is to assess whether the CAEs in the experiment would be expected to cause significant ion heating [6]. Reference [6] presents the results of full-orbit simulations of thermal ions in the presence of multiple CAEs, showing heating via stochastic velocity space diffusion. The ion heating rate is predicted versus mode amplitude in terms of $\delta b_\perp / B_0$. The CAE amplitudes in the experiment ($f > 600$ kHz) have values in the range $2 \times 10^{-4} < \delta b_\parallel / B_0 < 7 \times 10^{-4}$, which can be used to estimate the range of values for $\delta b_\perp / B_0$. Using the assumed valued of $k_\parallel / k_\perp$ from the simulation, $0.2 < k_\parallel / k_\perp < 0.5$, and the approximations $\delta b_\parallel / B_0 = \delta n / n_e$ and $\delta b_\perp / B_0 \sim \frac{k_\parallel}{k_\perp} \frac{\delta b_\parallel}{B_0}$, gives $0.4 \times 10^{-4} < \delta b_\perp / B_0 < 3.5 \times 10^{-4}$. This implies a relatively insignificant heating rate of $dT_i/dt < \sim 1$ keV s^{-1}. For the discharge where these modes are observed, $T_i \sim 900$ eV, so $T_i / (dT_i/dt) \sim 1$ s, which is much greater than the energy confinement time for the discharge. Also, of course, this heating

rate is actually an upper bound since the simulation assumes 21 modes, many more than the 7 observed CAEs in this discharge. Reference [6] does not discuss the dependence of the heating rate on number of modes.

5. Conclusions

In summary, analysis of reflectometry measurements is performed for CAEs and GAEs observed in an NSTX-U high power beam-heated discharge using a novel technique that inverts the measurements to obtain the density perturbation structure and amplitude of the modes. The results of inversion have multiple potential impacts including understanding the role of CAEs and GAEs in ion heating [6], energy transport [9] and anomalous electron thermal transport [7, 12]. It is found, for instance, that the results of the inversion yield cutoff displacements (d) larger than the mirror approximation estimates (d_{eff}) reported in [12]. However, even taking into account the larger values for cutoff displacement, the GAEs in the discharge considered have do not have sufficient amplitude to explain the anomalous electron thermal transport typical for the kind of discharge in which they were observed. It is also found that previous predictions of energy transport by CAEs [9, 10] likely over-predict the energy transport and that the CAEs have sufficiently low amplitudes to expect insignificant ion heating [6].

Acknowledgments

ORCID iDs

N.A. Crocker ⓘ https://orcid.org/0000-0003-2379-5814

References

[1] Heidbrink W.W., Fredrickson E.D., Gorelenkov N.N., Rhodes T.L. and Van Zeeland M.A. 2006 *Nucl. Fusion* **46** 324–34
[2] Fredrickson E.D., Gorelenkov N.N. and Menard J. 2004 *Phys. Plasmas* **11** 3653–9
[3] Fredrickson E.D. *et al* 2011 *38th EPS Conf. on Plasma Physics (Strasbourg, France, 27 June–1 July 2011)* vol 35G P2.119 (http://ocs.ciemat.es/EPS2011PAP/)
[4] Fredrickson E.D. *et al* 2011 *Proc. of 23rd IAEA Fusion Energy Conf. (Daejon, Korea, 11–16 October 2010)* EXW/P7-06 (www-naweb.iaea.org/napc/physics/FEC/FEC2010/html/fec10.htm)
[5] Stutman D., Delgado-Aparicio L., Gorelenkov N., Finkenthal M., Fredrickson E., Kaye S., Mazzucato E. and Tritz K. 2009 *Phys. Rev. Lett.* **102** 115002
[6] Gates D.A., Gorelenkov N.N. and White R.B. 2001 *Phys. Rev. Lett.* **87** 205003
[7] Gorelenkov N.N., Stutman D., Tritz K., Boozer A., Delgado-Aparicio L., Fredrickson E., Kaye S. and White R. 2010 *Nucl. Fusion* **50** 84012
[8] Kolesnichenko Y.I., Yakovenko Y.V. and Lutsenko V.V. 2010 *Phys. Rev. Lett.* **104** 75001
[9] Belova E.V., Gorelenkov N.N., Fredrickson E.D., Tritz K. and Crocker N.A. 2015 *Phys. Rev. Lett.* **115** 15001
[10] Belova E.V., Gorelenkov N.N., Crocker N.A., Lestz J.B., Fredrickson E.D., Tang S. and Tritz K. 2017 *Phys. Plasmas* **24** 42505
[11] Crocker N.A. *et al* 2011 *Plasma Phys. Control. Fusion* **15** 105001
[12] Crocker N.A. *et al* 2013 *Nucl. Fusion* **53** 43017
[13] Ono M. *et al* 2000 *Nucl. Fusion* **40** 557–61
[14] Sanz J.S., Hartfuss H.J., Anabitarte E., Navarro A.P., W VII-AS Team, NBI Team, Pellet Injection Team and ECRH Group 1990 *Nucl. Fusion* **30** 2383–91
[15] Kramer G.I., Sips A.C.C. and Cardozo N.J.L. 1993 *Plasma Phys. Control. Fusion* **35** 1685–99
[16] Colton A. and Cripwell P.J. 1992 *1992 IAEA Technical Committee Meeting, Microwave Reflectometry for Fusion Plasma Diagnostics (Abingdon, England, 4–6 March 1992)* (Vienna: IAEA) pp 157–67 (http://iaea.org/inis/collection/NCLCollectionStore/_Public/25/026/25026906.pdf)
[17] Colton A., Cripwell P.J., Kramer G.J., Sips A.C.C. and JET Team 1992 *JET Reports* JET-P(92)36 EUROfusion Scientific Publications (http://euro-fusionscipub.org/wp-content/uploads/2014/11/JETP920361.pdf)
[18] Podestà M. *et al* 2012 *Nucl. Fusion* **52** 94001
[19] Sabbagh S.A. *et al* 2002 *Phys. Plasmas* **9** 2085–92
[20] Sabbagh S.A. *et al* 2006 *Nucl. Fusion* **46** 635–44
[21] Lao L.L., John H., Stambaugh R.D., Kellman A.G. and Pfeiffer W. 1985 *Nucl. Fusion* **25** 1611–22
[22] Leblanc B.P., Diallo A., Labik G. and Stevens D.R. 2012 *Rev. Sci. Instrum.* **83** 10D527
[23] Nazikian R., Kramer G.J. and Valeo E. 2001 *Phys. Plasmas* **8** 1840–55
[24] Shampine L.F. 2008 *J. Comput. Appl. Math.* **211** 131–40
[25] Winsor N., Johnson J.L. and Dawson J.M. 1968 *Phys. Fluids* **11** 2448–50
[26] Nazikian R. *et al* 2003 *Phys. Rev. Lett.* **91** 125003
[27] De Boor C. 1978 *A Practical Guide to Splines (Applied Mathematical Sciences* vol 27) (New York: Springer)
[28] Reinsch C.H. 1971 *Numer. Math.* **16** 451–4
[29] Bell R.E. and Feder R. 2010 *Rev. Sci. Instrum.* **81** 10D724